International Journal of Extreme Manufacturing

PAPER • OPEN ACCESS

Near-zero-adhesion-enabled intact wafer-scale resist-transfer printing for high-fidelity nanofabrication on arbitrary substrates

To cite this article: Zhiwen Shu *et al* 2024 *Int. J. Extrem. Manuf.* **6** 015102

View the article online for updates and enhancements.

You may also like

- Controlled vapor growth of 2D magnetic Cr_2Se_3 and its magnetic proximity effect in heterostructures
Danliang Zhang, , Chen Yi et al.

- Development of line abnormal diagnosis system for overhead transmission lines
Bocheng Li, Jie Niu, Zhiqiang He et al.

- Analysis on Management Strategy of Lightning Protection in Hunan Distribution Lines
Jin-liang Li, Miao Zhao, Xiao-rong Chen et al.

This content was downloaded from IP address 110.191.72.199 on 06/11/2023 at 01:17

OPEN ACCESS
IOP Publishing | IMMT International Journal of Extreme Manufacturing
Int. J. Extrem. Manuf. 6 (2024) 015102 (14pp) https://doi.org/10.1088/2631-7990/ad01fe

Near-zero-adhesion-enabled intact wafer-scale resist-transfer printing for high-fidelity nanofabrication on arbitrary substrates

Zhiwen Shu[1,2,5], **Bo Feng**[1,2,5], **Peng Liu**[3], **Lei Chen**[1,2], **Huikang Liang**[1,2], **Yiqin Chen**[1,2,4], **Jianwu Yu**[1] and **Huigao Duan**[1,2,4,*]

[1] College of Mechanical and Vehicle Engineering, National Engineering Research Centre for High Efficiency Grinding, Hunan University, Changsha 410082, People's Republic of China
[2] Greater Bay Area Institute for Innovation, Hunan University, Guangzhou 511300, People's Republic of China
[3] School of Mechanical Engineering, Hunan University of Science and Technology, Xiangtan 411201, People's Republic of China
[4] Shenzhen Research Institute, Hunan University, Shenzhen 518000, People's Republic of China

E-mail: duanhg@hnu.edu.cn

Received 10 August 2023, revised 7 September 2023
Accepted for publication 9 October 2023
Published 3 November 2023

Abstract

There is an urgent need for novel processes that can integrate different functional nanostructures onto specific substrates, so as to meet the fast-growing need for broad applications in nanoelectronics, nanophotonics, and flexible optoelectronics. Existing direct-lithography methods are difficult to use on flexible, nonplanar, and biocompatible surfaces. Therefore, this fabrication is usually accomplished by nanotransfer printing. However, large-scale integration of multiscale nanostructures with unconventional substrates remains challenging because fabrication yields and quality are often limited by the resolution, uniformity, adhesivity, and integrity of the nanostructures formed by direct transfer. Here, we proposed a resist-based transfer strategy enabled by near-zero adhesion, which was achieved by molecular modification to attain a critical surface energy interval. This approach enabled the intact transfer of wafer-scale, ultrathin-resist nanofilms onto arbitrary substrates with mitigated cracking and wrinkling, thereby facilitating the *in situ* fabrication of nanostructures for functional devices. Applying this approach, fabrication of three-dimensional-stacked multilayer structures with enhanced functionalities, nanoplasmonic structures with ~10 nm resolution, and MoS_2-based devices with excellent performance was demonstrated on specific substrates. These results collectively demonstrated the high stability, reliability, and throughput of our strategy for optical and electronic device applications.

[5] These authors contributed equally to this work.
[*] Author to whom any correspondence should be addressed.

Original content from this work may be used under the terms of the Creative Commons Attribution 4.0 licence. Any further distribution of this work must maintain attribution to the author(s) and the title of the work, journal citation and DOI.

© 2023 The Author(s). Published by IOP Publishing Ltd on behalf of the IMMT

Supplementary material for this article is available online

Keywords: resist-based transfer printing, near-zero adhesion, critical surface energy, wafer-scale nanofabrication, *in situ* fabrication, optoelectronic devices

1. Introduction

The rapid advancement in high-resolution fabrication and transfer of nanoscale functional structures is driven by the demand for superior mechanical robustness and reliability, large-area uniformity, fast processing rates, all-dry processing conditions, low manufacturing costs, and crucially, conformal integration onto arbitrary substrates, including flexible, stretchable, and curvilinear surfaces, without compromising performance [1–9]. This demand is driven by the fast-growing need for unconventional form factors in broad applications, including artificial skin [1], brain/machine interfaces [2], rollable and full-color displays [5, 10], three-dimensional (3D)-stacked multilayer functional nanostructures, and heterodevices [11–15].

Direct conformal printing technology provides a fast, reliable, and simple method for the realization of curved surface electronics and functional circuits with a 3D free-form surface [16–19]. However, because of technical limitations, it is currently only suitable for printing micro- or even millimeter scale structures. Nanostructure-based nanotransfer printing (nTP) is the most commonly used process for preparing nanostructures on substrates that are incompatible with conventional lithography processes. This approach is particularly relevant to structures based on electron-beam lithography (EBL), which require extremely flat, smooth, and conductive substrates. Nanostructure-based nTP methods developed thus far include direct kinetically controlled, 'pick and place' printing [4], template-assisted transfer printing [20–23], bottom- or top-sacrificial-layer-assisted processes [7, 22, 24, 25], thermal-release transfer printing [26, 27], water-assisted transfer printing [28], laser-assisted transfer printing [29, 30], and many others [31, 32]. These methods facilitate the direct integration of diverse micro- or nanostructured materials into 2D- and 3D-organized patterns, and are promising candidates for the controlled fabrication of multilayer functional nanostructures and 3D-stacked devices on any required solid surface [15, 22, 27, 33, 34].

Outstanding challenges must be addressed to ensure the optimal performance of optical and electronic devices in the process of intact peeling and release of large-area nanostructures. First, during the implementation of the current nanostructure-based nTP, nanostructures are initially generated through standard lithography techniques on donor substrates and subsequently released onto other receiver substrates using a viscoelastic stamp (such as polydimethylsiloxane (PDMS) [4] or silk fibroin [2]) as a transfer medium. The transfer-printing process generally involves competition between adhesion forces at two interfaces: the pattern/stamp interface and the substrate/pattern interface. Considerable effort [35, 36] has been dedicated to improving the performance of the former in the peeling process: for example, researchers have sought to optimize stamp adhesion and even develop smart stamps. However, stamping techniques are typically limited to isolated or micrometer-sized structures [37, 38], and the reliable transfer printing of large-area and 10 nm nanostructures remains a fundamental challenge. The complete stripping of nanoscale structures is much more challenging than that of micrometer-scale or larger structures owing to the limited contact area between the stamp and nanostructure. Moreover, increased stamp adhesion results in elevated stress levels during the peeling process, which leads to stress instabilities that hinder high-fidelity pattern transfer. These strategies inevitably increase the difficulty of the subsequent post-release process, even at low release velocity [4, 39]. In addition, a layer of polymer (such as polymethyl methacrylate (PMMA) or polyvinyl alcohol) is spun on top of the pattern to conformally coat the nanostructure. This ensures that the nanostructure peels off more effectively. However, high fidelity is still difficult to guarantee during the release and removal of the polymer, particularly for large areas at a scale of ∼10 nm.

The second main challenge is the strong adhesion of the substrate/pattern interface induced by the inherent surface energy of the hard donor substrate. This inevitably causes heavy cross-linking between the targets and the donor substrate. During the process of stripping the targets from a donor substrate to a viscoelastic stamp, sacrificial underlayers (such as metals [24] or polymers [38]) are typically used to reduce the binding force between the pattern and substrate. However, this approach increases the complexity of the process and may result in surface contamination or material damage during subsequent wet-etching steps. A further challenge relates to nanostructure-based transfer printing being essentially an *ex situ* manufacturing process for the target substrate, which means that the adhesion between the patterns and the target substrate can only be controlled using post-processing techniques. For the above-mentioned reasons, achieving high-fidelity transfer of large areas of nanostructures to the target substrate during release remains challenging, with specific issues encountered of nanopixel loss, misalignment, distortion, and low throughput. Consequently, there is an urgent need for a novel approach to circumvent these limitations.

Here, considering that the resist is the basis for obtaining nanopatterns, we proposed a wafer-scale, resist-based nTP paradigm that was realized by transferring the resist nanofilms instead of directly transferring the structures. Compared with conventional nanostructure-based nTP processes, this new paradigm simplified transfer printing while realizing *in situ* and high-fidelity fabrication of large-area nanostructures on difficult-to-process substrates. We demonstrated a

sacrificial-layer-free and all-dry near-zero-adhesion to achieve intact peeling and release of wafer-level resist nanofilms onto arbitrary substrates without wrinkles, cracks, or defects. A critical surface energy interval was attained through single-molecule surface modification. This minimized the interfacial adhesion force between the resist nanofilm (e.g. PMMA) and the donor substrate to guarantee complete pre-definition while ensuring the intact stripping and post-release of the resist nanofilms. We explained the mechanism based on measurements of wettability and mechanical simulations. We also demonstrated that this fabrication strategy can be used to effectively prepare multiscale nanostructures, such as 3D-stacked multilayer hierarchies, ultrasmall metallic nanogaps, and patterns. Additionally, it enabled the creation of optoelectronic devices with exceptional reliability and responsiveness on arbitrary substrates. The method reported in this work will facilitate the monolithic integration of nanoscale functional materials with next-generation nanophotonic and electronic devices on arbitrary substrates at a larger scale than the currently achievable.

2. Results and discussion

To demonstrate the benefits of our resist-based nTP technique for unconventional substrate fabrication, we initially compared it with the nanostructure-based nTP method, as illustrated in figures 1(a) and (b). Figure 1(a) depicts one of the most frequently used techniques in nanostructure-based nTP, which involves bottom-sacrificial-layer technology. This *ex situ* deposition manufacturing method for the target substrate necessitates wet etching of the sacrificial layer, which results in defects on the target substrate, such as pixel loss (figure 1(a-x)), misalignment (figure 1(a-xi)), and distortion (figure 1(a-xii)). Figure 1(b) shows the process flow of our proposed resist-based nTP technology, which is an all-dry process that eliminates the need for sacrificial layers. This innovative approach uses an adhesion-free PDMS stamp and dynamic control of interface adhesion. The crucial step in the entire process is the modification of the surface of the donor substrate at the single-molecule level to achieve a critical surface energy interval (step i). Then, an ultrathin PMMA nanofilm is uniformly spin-coated onto the pre-modified substrate, where the adhesion force approaches zero (step ii). This is followed by exposure and development steps (step iii). Subsequently, a PDMS viscoelastic stamp is applied directly onto the PMMA film to create a new laminate with interfacial adhesion solely dependent on van der Waals forces [7]. Thereafter, the fully laminated PDMS/PMMA film is subsequently delaminated from the rigid donor surface with an extremely low stripping force and directly transferred onto the receiver substrate through printing (steps iv and v). After undergoing a post-thermal release process, the modification-free PDMS stamp is automatically released, and a large-area PMMA nanofilm without cracks, wrinkles, or deletions is transferred onto any desired surface (step vi). Next, the target substrate is subjected to *in situ* deposition for direct pattern functionalization (step vii). Finally, large-area multiscale nanostructures are fabricated on the target substrate after the lift-off process (step viii).

As shown in table 1, our method differs from structure-based nTP in its use of *ex situ* lithography and *in situ* deposition. This enables fabrication of flat and hard substrates, provides compatibility with the final substrate, and avoids damage to the final material or device caused by high-energy beams. By contrast, *in situ* deposition ensures high fidelity, strong adhesion, and high resolution of the structure on the target substrate. A specific comparison of the two approaches is provided in table S1, which shows that our method has better overall performance.

Achieving intact stripping requires near-zero adhesion between the PMMA resist and donor substrate, which can be achieved through pre-treatment and functionalization with single molecules. This results in a minimum adhesion force between the precisely pre-coated resist nanofilm and the donor substrate. Although a lower surface energy is generally advantageous for intact stripping, there is a paradox in that the formation of a complete PMMA film must first be achieved, and an excessively low substrate surface energy may impede the formation of the PMMA resist film (figure 1(c-i)). The excessive surface energy of the substrate may result in wrinkles, damage, and other defects (figure 1(c-ii)) during peeling or even prevent peeling (figure 1(c-iii)). A critical surface-energy threshold must be met to achieve damage-free peeling and complete formation of the PMMA resist film (figure 1(c-iv)). The corresponding experimental images are shown in figure S1.

Figure 1(d) shows comparisons of optical photographs and atomic force microscope (AFM) images of the two laminates for PMMA/PDMS with (i, ii) and without (iii, iv) a near-zero adhesion force at the resist nanofilm/silicon interface during peeling. The near-zero adhesion engineered by single-molecule modification (i, ii) helped to achieve intact peeling of the wafer-scale and ultrafine resist nanofilm and reduce the surface roughness (R_a) to 3.2 nm. By contrast, because the surface of the hard silicon wafer was functionalized with an insufficient number of single molecules (iii, iv), its remaining surface energy was still large, which prevented the silicon/PMMA interfacial adhesion force from reaching a critical value. Therefore, in the stripping process, a larger stripping speed was required to peel off the PMMA, which led to a large deformation of the PDMS and a stress mismatch between the PDMS and PMMA layers. This effect led to undesirable properties, including a high surface roughness ($R_a = 29.0$ nm), poor uniformity, and wrinkling in the peeling process. We also measured the surface roughness of the directly spin-coated PMMA and that of the intact transferred PMMA to be 0.24 nm and 0.38 nm, respectively, as shown in figure S2. These results confirmed that the intact transferred PMMA also had a high surface quality.

To verify the reliability and reproducibility of this method, the thickness of the spin-coated PMMA nanofilm was shrunk to 90 nm (figure S3), and the peeling process of PMMA nanofilms was repeated an additional 30 times on an identically pre-rendered substrate (figure S4). Our resist-based nTP technique exhibited the notable advantages of acceptable reproducibility, high stability, and high throughput. Furthermore, no external thermal budgets [12] were

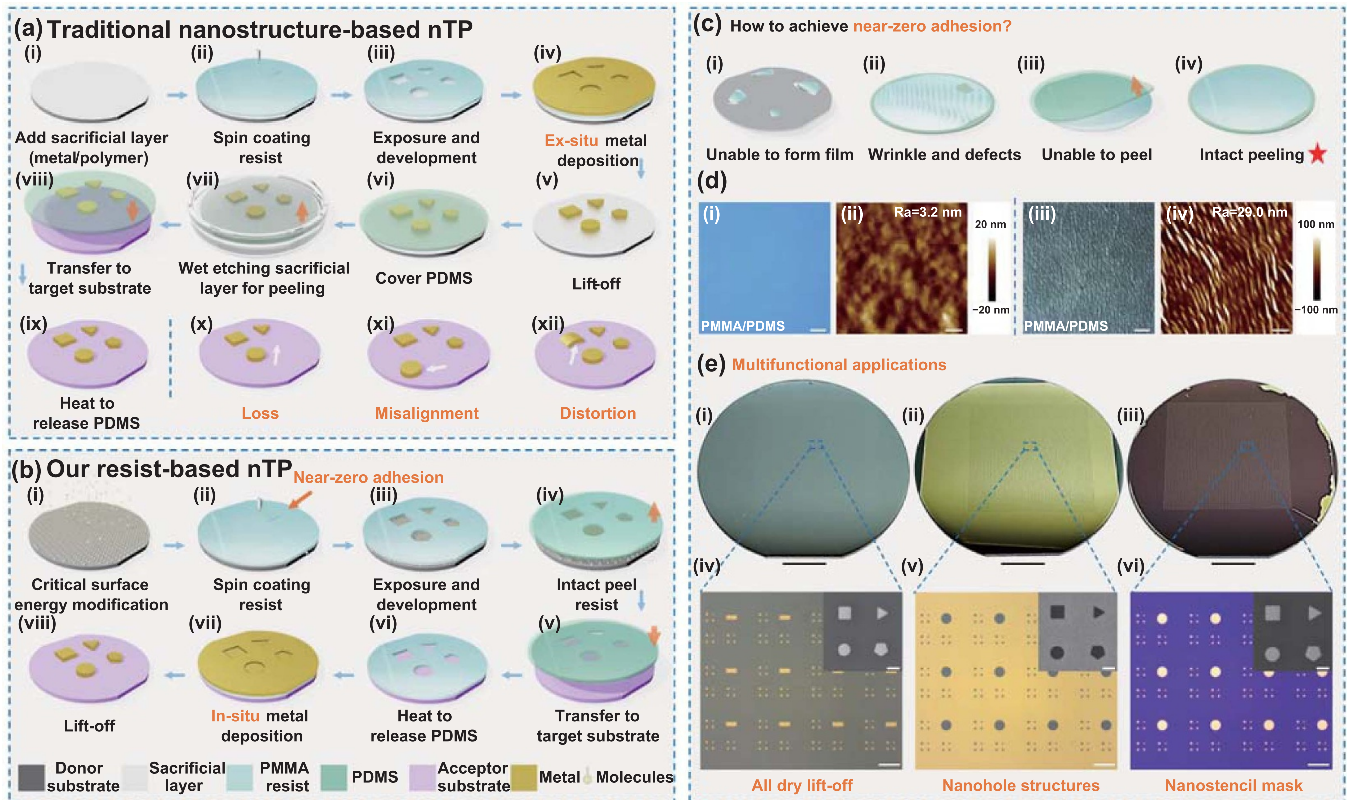

Figure 1. Schematic illustrations and demonstrations of the benefits of our near-zero-adhesion-enabled resist-based nTP technique based on critical interface adhesion. (a) Schematic diagram of traditional nanostructure-based nTP methods. (b) Schematic diagram of our proposed resist-based nTP method. (c) Comparison of spin coating and transfer of the resist film with different degrees of molecular modification. (d) Optical microscope images and AFM images: (i, ii) intact peeling of a PMMA film with a surface roughness (R_a) of 3.2 nm and (iii, iv) incomplete peeling of a PMMA film with a surface roughness of 29.0 nm. (e) Demonstration of the process for fabricating multiscale structures on a 2-inch silicon or silicon oxide wafer: (i) all-dry lift-off process; (ii) preparation of nanohole structures via the contour-exposure strategy; (iii) the use of nanostencil masks; and (iv–vi) corresponding local optical and SEM micrographs. Scale bars: 1 cm in (e-i)–(e-iii), 200 μm in (d-i), (d-iii) and (e-iv)–(e-vi), 10 μm in (d-ii), (d-iv), and 500 nm in the insets of (e-iv)–(e-vi).

Table 1. Comparison between traditional nanostructure-based nTP techniques and our proposed resist-based nTP technique for nanofabrication.

For the target substrate	Nanostructure-based nTP	Resist-based nTP
Property	*Ex situ* lithography & *ex situ* deposition	*Ex situ* lithography & *in situ* deposition
Fidelity	Low (loss, misalignment, distortion)	High
Adhesion	Weak	Strong
Resolution	Low	High
Range of applications	Single	Multiple e.g. nanostencil mask and all dry lift-off

embedded in the peeling procedure, which further improved its reliability.

Our proposed resist-based transfer technology offers considerable advantages for various applications because of its near-zero adhesion properties. Specifically, the approach can be used for all-dry lift-off to prepare nanocolumn structures and nanohole structures. Furthermore, nanostructures may be fabricated on challenging substrates using a nanostencil mask (figure S5). We demonstrate the fabrication of each of these three multiscale array structures on 2-inch wafers, as shown in figure 1(e-i)–(e-iii). The structures ranged in size from 400 nm to 100 μm (figure 1(e-iv)–(e-vi)). These results demonstrate the multifunctional capabilities of our method and its high processing efficiency, as detailed in the following.

As previously mentioned, the achievement of a near-zero adhesion force at the interface between the nanofilm and donor substrate is crucial for the successful peeling of wafer-scale resist nanofilms onto PDMS stamps. In addition, to gain a deeper understanding of the mechanism by which a critical surface energy interval was achieved on rigid silicon surfaces through single-molecule modification, we measured the wettability of octadecyltrichlorosilane (OTS)-decorated surfaces and carried out simulations involving mechanical forces for the peeling of resist nanofilms, as illustrated in figure 2. The

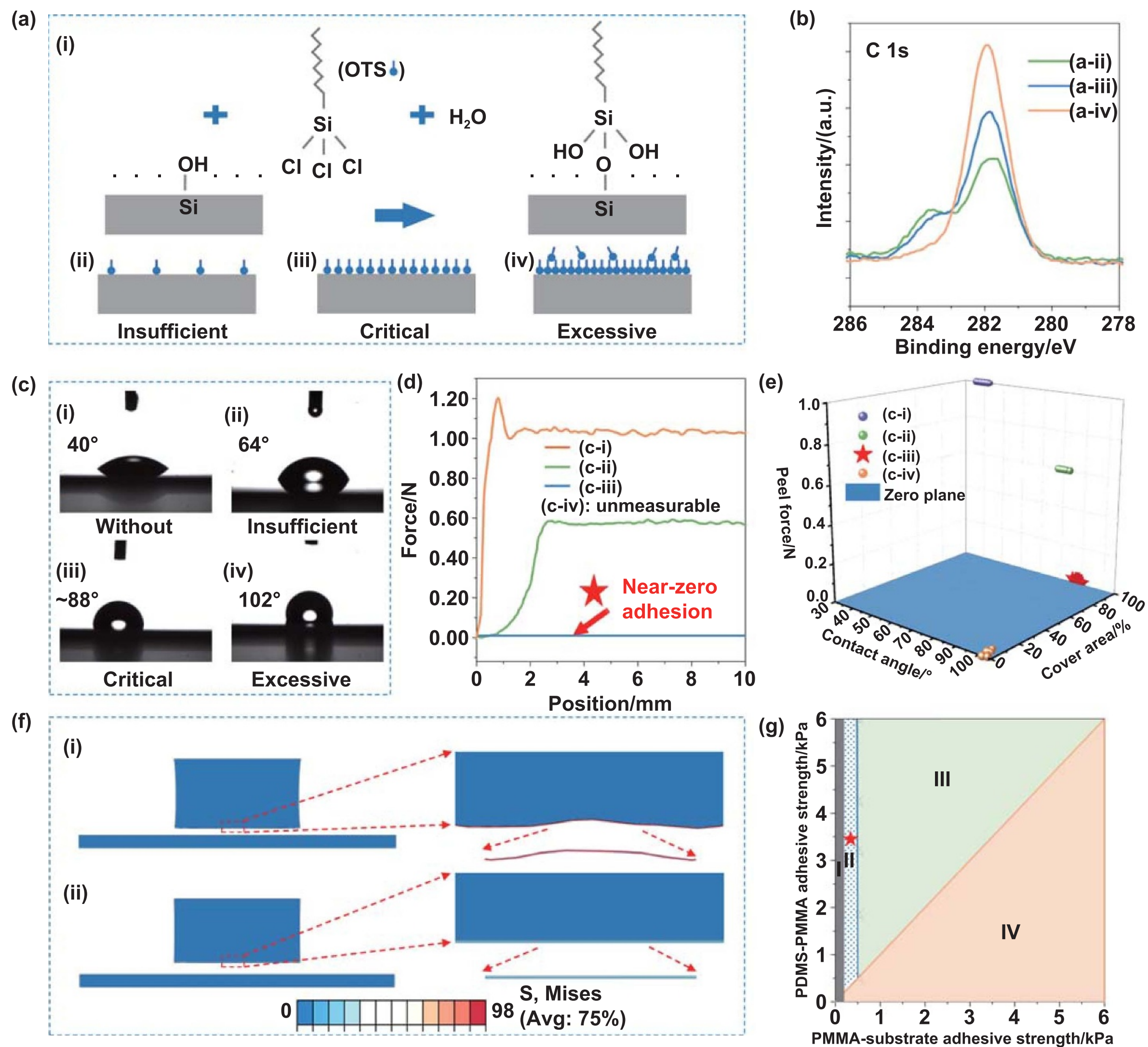

Figure 2. Schematic representation of the mechanism of achieving near-zero adhesion and intact transfer based on OTS surface modification. (a) Schematic diagram of the mechanism of critical surface-energy modification: (i) absorption of OTS molecules onto a silicon surface; (ii) pre-treated silicon surfaces with insufficient OTS modification; (ii) critical OTS modification; and (iv) excessive OTS modification. (b) XPS measurements of single-molecule adsorption with different degrees of modification. (c) Contact angle of water molecules on the silicon surface under different OTS modification conditions: (i) without OTS modification; (ii) with insufficient OTS modification; (iii) with critical OTS modification; (iv) with excessive OTS modification. (d) Measurement of the mechanical force for peeling PMMA films from the substrate surface for different OTS modification conditions. (e) Relationship between the peeling force, contact angle, and PMMA coverage area. (f) Stress nephogram obtained from finite-element analysis of the stripping process: (i) non-intact peeling and (ii) intact peeling. (g) Finite element simulation to determine the critical surface-energy interval. The phase diagram for the stripping results of the nanofilm dominated by the adhesive strength at the PMMA/substrate and PDMS/PMMA interfaces: (i) unable to form a film; (ii) near-zero-adhesion and intact-peeling interval; (iii) non-intact-peeling interval; and (iv) unable to peel.

silicon-wafer surface in the air was inherently hydrophilic owing to the presence of hydroxyl groups. To ensure the complete pre-definition of a large-scale PMMA nanofilm on the substrate, additional surface pre-treatment was necessary to impart suitable surface energy, wettability, and adhesion force to the film. OTS molecules exhibit selective reactivity toward hydroxyl groups, resulting in the formation of covalent bonds (Si–O–Si) on the substrate surface. They can also react with water molecules in the atmosphere to convert Si–Cl bonds to Si–OH bonds [40–44], as shown in figure 2(a-i). Accordingly, by controlling the specific modification time at room temperature (see methods), different absorption states for OTS molecules with insufficient absorption, critical absorption, and excessive absorption can be decorated on the wafer surface, as illustrated in figure 2(a-ii)–(a-iv), respectively. The intensity of the C 1 s binding energy for the different degrees of modification was characterized using x-ray photoelectron spectroscopy (XPS). This revealed that the duration of modification influenced the adsorption capacity of single molecules on the substrate, as shown in figure 2(b).

Figure 2(c) shows the contact angle of water molecules on the silicon surface (i.e. the wettability of the silicon surface) under different OTS modification conditions; these values were used to characterize the surface energy. In addition,

the wettability of anisole and PMMA is shown in figures S6 and S7. An appropriate OTS modification time can lead to the contact angle being within a critical range, which is represented by the average value of multiple measurements (∼88°). The critical contact angle helps to achieve a critical surface energy interval on the wafer surface, which, in turn, minimizes the adhesion between the PMMA nanofilm and the silicon substrate. This enables complete pre-coating and stripping of wafer-scale ultrathin PMMA (130 nm and below).

The mechanical force for peeling the PMMA nanofilm from the substrate surfaces with different OTS modification conditions (figure 2(c-i)–(c-iii)) was measured, as plotted in figure 2(d). Through the use of near-zero mechanical force (0.01 N, blue curve), the intact PMMA nanofilm could be peeled from the silicon surface functionalized with OTS molecules with the critical modification status. The required stripping force for a 130 nm thick PMMA nanofilm was maintained at less than 0.02 N throughout 20 peeling cycles (figure S8). These results indicated the high stability of the surface. Furthermore, when the OTS modification conditions deviated from the critical range, such as a water contact angle of ∼64°, the PMMA nanofilm exhibited stronger adhesion with the silicon wafer, and a larger mechanical stripping force (0.6 N, green curve) needed to be applied to the PDMS stamp. This generated wrinkles, cracks, and defects, hindering the quality and uniformity of the stripped PMMA nanofilm. When a larger mechanical force of 1.0 N was applied to the stamp, the PMMA nanofilm could not be stripped from the silicon wafer where the surface was unmodified by OTS molecules (orange curve). For excessive modification, owing to poor wettability, PMMA could not form a film. Therefore, it was not possible to measure the peeling force in this case. Nevertheless, the peeling force was less than that of the critical state (i.e. $<$0.02 N).

By integrating the findings from figures 2(c) and (d), a comprehensive depiction of the correlations among the peeling force, contact angle, and covered area is presented in figure 2(e). A near-zero-adhesion force could only be achieved at the critical surface energy interval (c-iii), at which the PMMA coverage area reached 100%. Thus, we can establish a solid foundation for intact-transfer-printing technology based on the resist film. The stress nephogram obtained from the mechanical simulation (figure 2(f)) indicates that the stress experienced by intact transfer (ii) was substantially lower than that of non-intact transfer (i), thereby preventing wrinkle formation. Interface adhesion plays a dominant role in determining these distinct outcomes. Figure 2(g) illustrates the results from the qualitative simulation of the peeling process obtained through finite element analysis. As previously mentioned, this mechanical process involves competition between the adhesive strength of the PMMA/substrate and PDMS/PMMA interfaces. The adhesive strength in the former (X-axis in figure 2(g)) is determined by the OTS-modification conditions. However, the adhesive strength in the latter (Y-axis in figure 2(g)) is dominated by the viscosity and surface energy of the elastomeric PDMS stamps, and is usually less than 6 kPa, according to previous works [45]. Accordingly, when the adhesive strength at the PMMA/substrate interface is less than or equal to the critical value of ∼0.5 kPa (corresponding to the critical OTS-modification status for the wafer surface), intact peeling cannot be easily achieved, as plotted in region II (we note that region I corresponds to the inability of PMMA to form membranes). With increasing adhesive strength at the PMMA/substrate interface, incomplete peeling (region III) of the PMMA nanofilm with wrinkles takes place. Region IV indicates that the nanofilm cannot be stripped from the donor substrate. The corresponding mechanical simulation model is shown in figure S9.

To demonstrate the use of our nTP technique to realize functional 2D and 3D nanostructures on arbitrary receiver surfaces, we first prepared a wafer-scale, single-layer PMMA nanofilm on a SiO_2/Si substrate, as shown in figure 3(a). Figure 3(a-i) illustrates a complete PDMS/PMMA laminate stripped from a 4-inch donor silicon wafer with critical surface energy interval at room temperature. Subsequently, this laminate (i.e. PDMS-supported PMMA nanofilm) was directly printed on the 300 nm-SiO_2/Si wafer surface. After heating, the modification-free PDMS was released owing to the differences in the thermal expansion coefficient and elastic moduli of the different materials. This large-scale PMMA nanofilm was free from cracks, wrinkles, and deletions (figure 3(a-ii)). We note that this low-temperature release process is fully compatible with the back-end-of-line process in traditional silicon CMOS process flows. The whole process of intact peeling and release of the PMMA nanofilm is also shown in movie S1. The mean and standard deviation of the PMMA thicknesses measured at 25 different regions on the SiO_2/Si substrate were 135.8 nm and 0.85 nm, respectively (figure 3(a-iii)), indicating that the nanofilm released on the SiO_2/Si wafer was uniform and stable.

To further demonstrate the capabilities of this technique, we fabricated metal–dielectric–metal Fabry–Pérot (Ag/PMMA/Ag) cavities on a flexible polyethylene terephthalate (PET) substrate, as schematically shown in figure 3(b-i). The PMMA nanofilm, in conjunction with the metal laminate, functioned as a wavelength selector based on the resonance modes within the Fabry–Pérot cavity. When the PET substrate was bent to 45°, the transmitted color changed from red to a gradient ramp from the middle to the sides, owing to the variation of the incidence angle [46]. This explains the change in the transmission spectra observed in figure 3(b-ii). Furthermore, the measured transmission spectra of Ag/PMMA/Ag cavities with PMMA thicknesses of 170, 250, and 300 nm are plotted in figure 3(b-iii). A normalized transmittance greater than 50% could be achieved with wavelengths of 449 nm (blue), 550 nm (green), and 650 nm (red) by adjusting the thickness of the transferred PMMA nanofilm. This confirms that the fabricated nanostructure functions as a high-quality color filter, which can be applied in multispectral or color-temperature sensors. More details are shown in figure S10 in the supporting information.

Heterostructures created by stacking layers of nanofilms (e.g. complex-oxide materials [12]) exhibit a vast range of functional properties that are desirable for next-generation electronic, energy-conversion, and energy-storage devices. However, robust and reliable methods for fabricating such

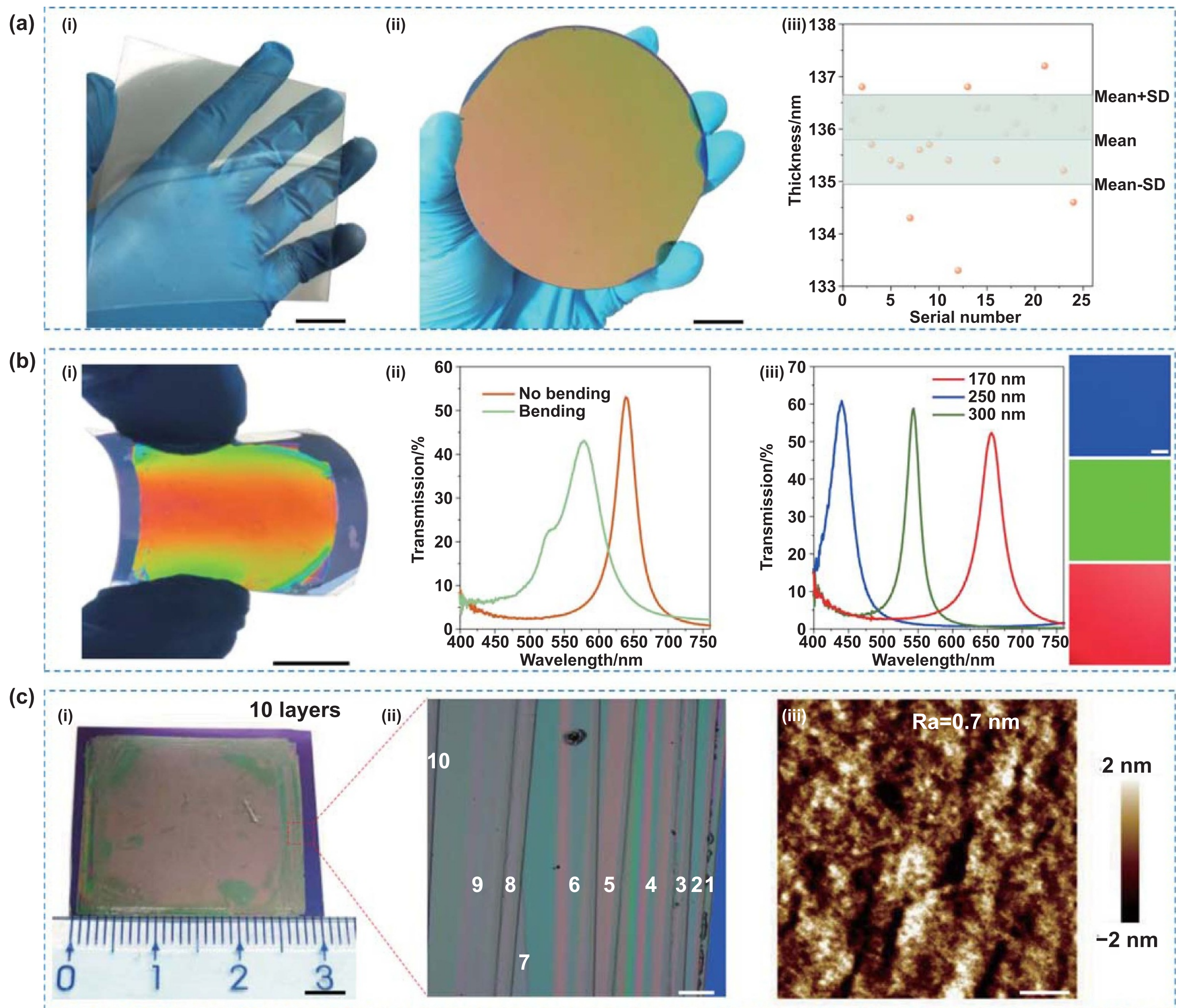

Figure 3. Demonstration of 2D and 3D functional resist nanofilm systems formed using our resist-based nTP technique. (a) Successful intact transfer printing of a 4-inch single layer of PMMA with a thickness of 130 nm: (i) 4-inch single-layer PMMA film on a PDMS stamp; (ii) the PMMA film released onto a 300 nm thick SiO_2/Si substrate; and (iii) the mean and standard deviation of the PMMA thicknesses measured at 25 different regions on the SiO_2/Si substrate. (b) Successful intact transfer printing to achieve a metal–dielectric–metal Fabry–Perot (Ag/PMMA/Ag) cavity: (i) fabricated Ag/PMMA/Ag cavity on a flexible PET substrate; (ii) measured transmission spectra by the cavity with 150 nm thick PMMA under horizontal and bending conditions; (iii) transmission spectra of Ag/PMMA/Ag cavities on a quartz substrate with PMMA thicknesses of 170, 250, and 300 nm. (c) Successful intact-transfer printing to achieve 3D stacking of 10 layers of PMMA: (i) optical images of 10 130 nm thick layers of PMMA nanofilm stacked on the SiO_2/Si substrate; (ii) enlarged edge image of a 3D-stacked PMMA nanofilm; (iii) surface roughness of multilayer PMMA nanofilms stacked on the SiO_2/Si substrate. Scale bars: 5 μm in (c-iii), 200 μm in (b-iii) and (c-ii), 5 mm in (c-i), 1 cm in (b-i), 2 cm in (a).

heterostructures are urgently needed. Our resist-based nTP technique allows for integration with 3D-stacked multilayer resist nanofilms. By repeating the same intact ‘peeling and releasing’ processes (figure S11, supporting information), ten 130 nm thick layers of PMMA nanofilm were sequentially stacked on a SiO_2/Si substrate and microslide, as shown in (figure 3(c-i, ii)) and figure S12. The surface roughness of the multilayer PMMA nanofilms stacked on the SiO_2/Si substrate was maintained at $\sim$0.7 nm, confirming the excellent uniformity and reproducibility of this transfer-printing method (figure 3(c-iii)). In addition, no external solution was involved in the entire process, making it more robust, convenient, and at a lower cost than conventional methods [12].

To verify the resolution limit and throughput of our method, we fabricated different building blocks with multiscale gold structures on *in situ* donor substrates through all-dry lift-off, as shown in figure 4. Figure 4(a) represents the process flow for the preparation of multiscale gold structures using the all-dry peeling technique of PMMA nanofilms. A 350 nm thick bilayer of PMMA (200 nm (495 kDa) and 150 nm (950 kDa)) was first spin-coated on a silicon surface pre-modified with single molecules. The structures were then patterned on a

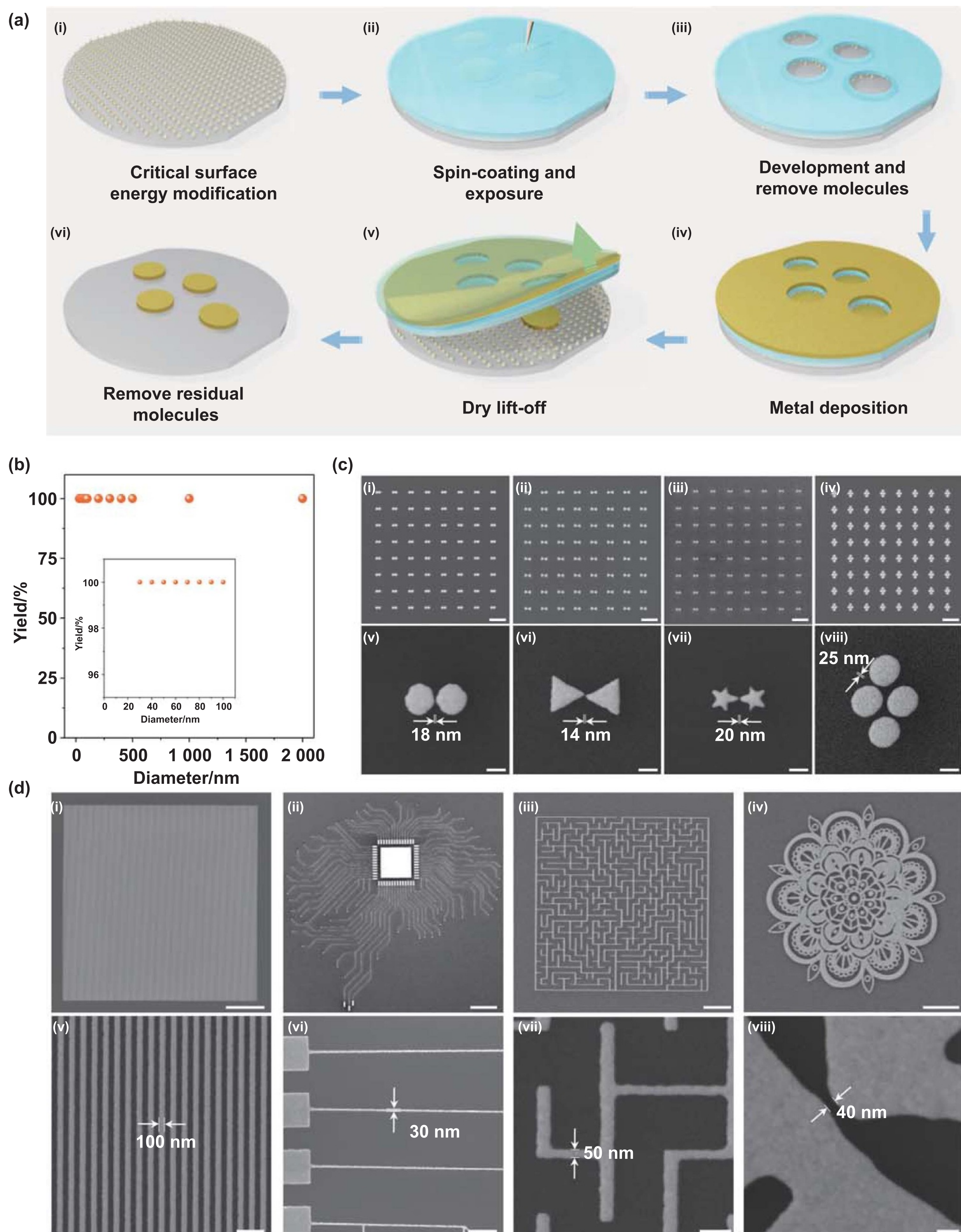

Figure 4. Demonstration of reliable patterning of various multiscale gold nanostructures on *in situ* donor substrates by all-dry lift off. (a) Flow chart of the fabrication steps: (i) surface modification to achieve critical surface energy interval; (ii) spin-coating of a 350 nm thick bilayer of PMMA (200 nm (495 kDa) on the bottom and 150 nm (950 kDa) on the top) and exposure; (iii) development and removal of exposed molecules using oxygen plasma; (iv) metal deposition; (v) dry lift-off using PDMS or tape; (vi) removal of residual molecules using oxygen plasma. (b) The yield of isolated gold disks with diameters ranging from 30 nm to 2 μm. (c) and (d) SEM images of different kinds of multiscale nanostructure on donor substrates after PMMA peeling. Scale bars: 100 nm in (d-viii), 200 nm in (c-v)–(c-viii) and (d-vii), 500 nm in (d-v), (d-vi), 2 μm in (c-i)–(c-iv) and (d-iii), 5 μm in (d-iv), and 10 μm in (d-i), (d-ii).

PMMA nanofilm using conventional EBL. After a 30 nm thick gold film was deposited, the sample was ready for the peeling of the PMMA nanofilm (figure 4(a-i)–(a-iv)). During the dry-peeling process, a modification-free PDMS stamp was pasted onto the gold film to form a new laminate. Using a mechanical force of less than 0.02 N, the PDMS/gold film/PMMA laminate was selectively stripped from the donor substrate (figure 4(a-v)), and the designed multiscale structures were intact and patterned onto the *in situ* substrate (figure 4(a-vi)). The yields of isolated gold disks with diameters ranging from 30 nm to 2 μm are shown in figure 4(b). For ultrathin metallic nanostructures as small as 30 nm, 100% peeling was obtained, indicating the high reliability and resolution of this transfer-printing technique. A more detailed characterization of the gold structures was then carried out using scanning electron microscopy (SEM, figure S13), which confirmed the absence of residual PMMA film on the substrate and gold disks.

The high process fidelity made it possible to fabricate multiscale plasmonic nanogaps with high resolution on arbitrary substrates, such as a gold bowtie array on a silicon wafer and a gold-disk array on an oxidized silicon substrate, as shown in figure 4(c-i)–(c-iv). Nanogaps are important building blocks that have great value in many applications, such as surface-enhanced Raman scattering (SERS) [47, 48] for molecular detection. The enlarged SEM image in figure 4(c-v)–(c-viii) shows a gap as low as 14 nm for the gold bowtie, suggesting a $\sim$10 nm resolution limit for the dry peeling of PMMA nanofilms. Figure 4(d-i)–(d-iv) shows various as-fabricated gold patterns (such as gratings, circuits, nanocodes, and nanopetals) with high density and large areas on donor silicon substrates. The zoomed-in SEM images in figure 4(d-v)–(d-viii) show that all nanostructures were intact and uniform throughout the whole process. This indicates high stripping accuracy and throughput during the peeling process of the PMMA nanofilms.

We also used our nTP technique to reliably fabricate different kinds of multiscale gold structures with features as low as tens of nanometers onto difficult-to-process receiver substrates that have poor compatibility with traditional EBL-based patterning, as shown in figure 5. This *in situ* deposition technique is compatible with all insulating and polymeric substrates. We note that our method simplifies the transfer process and serves as a nanostencil mask, avoiding issues associated with direct nanostructure-based nTP, such as structural loss, misalignment, distortion, and low throughput, to achieve high-fidelity structural transfer. A schematic illustration of the nanostencil-mask concept on an arbitrary substrate is depicted in figure 5(a). First, the designed multiscale pattern was prepared in a PMMA nanofilm on a donor substrate with critical surface energy interval using conventional EBL (steps i–iii). Upon peeling off, the PMMA pattern adhered to the elastomeric PDMS stamp (step iv) and was then printed onto arbitrary receiver substrates (e.g. a curvilinear surface, suspended substrate, and a flexible and stretchable substrate) after the thermal release of the stamp (steps v–viii); the experimental images are shown in figure S14. The gold film was deposited onto the receiver substrate *in situ* using the transferred PMMA pattern as a nanostencil mask [3]. When the nanostencil was removed via the aforementioned technique (figure 4(a)), it left gold nanostructures on the receiver substrate with shapes complementary to that of the apertures on the PMMA nanofilm-based nanostencil. The results shown in figure 5(b) demonstrate that well-defined multiscale gold nanostructures were completely transferred onto various surfaces, such as a gold bowtie array on a convex lens (i, ii), a gold disk array on a concave lens (iii, iv), free-standing nanoholes on a suspended substrate (v, vi), and a nanograting on flexible PDMS (vii, viii). In comparing the photographs of the receiver (figure 5(b-ii)) and donor substrates (figure 4(c-ii, vi)), no structural damage or breakage occurred, and the patterning resolution was maintained at $\sim$10 nm. This indicates the high reliability of *in situ* peeling and thermal release of the PMMA nanostencil for multiscale structures. The details of the 10 nm width nanogap on a curvilinear surface (figure 5(b-ii)) show that all nanobowtie arrays were intact, which confirms that there was no gap between the PMMA nanostencil and the curvilinear substrate. This suggests that our transfer-printing technique mitigates the shadowing effect [3], which results from factors such as uneven surface topology and bending or curving of the materials. The micrographs in figure 5(b-vi, viii) reveal the uniform widths of the nanoholes and gratings fabricated on suspended and elastic substrates. There was no observable overlap or displacement of the high-density pattern, proving the high fidelity of the whole fabrication strategy. This shows potential for biological DNA sequencing and flexible device applications.

This intact resist-based nTP technique, enabled by near-zero adhesion, is also compatible with contour exposure [7, 49]. This allows the building of large-area structures and devices at high yields, as depicted in figure 6. Figure 6(a) demonstrates the efficient *in situ* preparation of a 6.25-million-disk array with a diameter of 2 μm on a target substrate by combining our nPT technique with contour exposure. Figure 6(a-i) shows the patterned PMMA/PDMS laminate, which was stripped from the donor substrate. In the contour exposure process, the outline templates were rapidly patterned in the PMMA nanofilms coated on the silicon substrate with a critical surface energy interval. The exposure time and proximity effect of lithography were markedly lower than those of conventional lithography. A flow chart of the whole fabrication process is shown in figure S15. After the thermal release of the nanofilm, the PMMA pattern was successfully transferred onto a SiO_2/Si substrate as a reliable nanostencil, as shown in figure 6(a-ii). By repeating the gold deposition and dry-peeling procedures, the high-fidelity gold-disk array remained on the SiO_2/Si surface, as illustrated in figure 6(a-iii, iv). More details are shown in figure S16. Figure 6(b) shows the multiscale gold disks with diameters ranging from 200 nm to 200 μm on a 4-inch SiO_2/Si wafer. This reveals that this combined strategy has advantages for scale-up, such as high resolution, sufficient stability, excellent uniformity, and high throughput. More details are shown in figure S17. In addition, this strategy enables the fabrication of high- and low-density patterns on one substrate through a single all-dry process. This means that

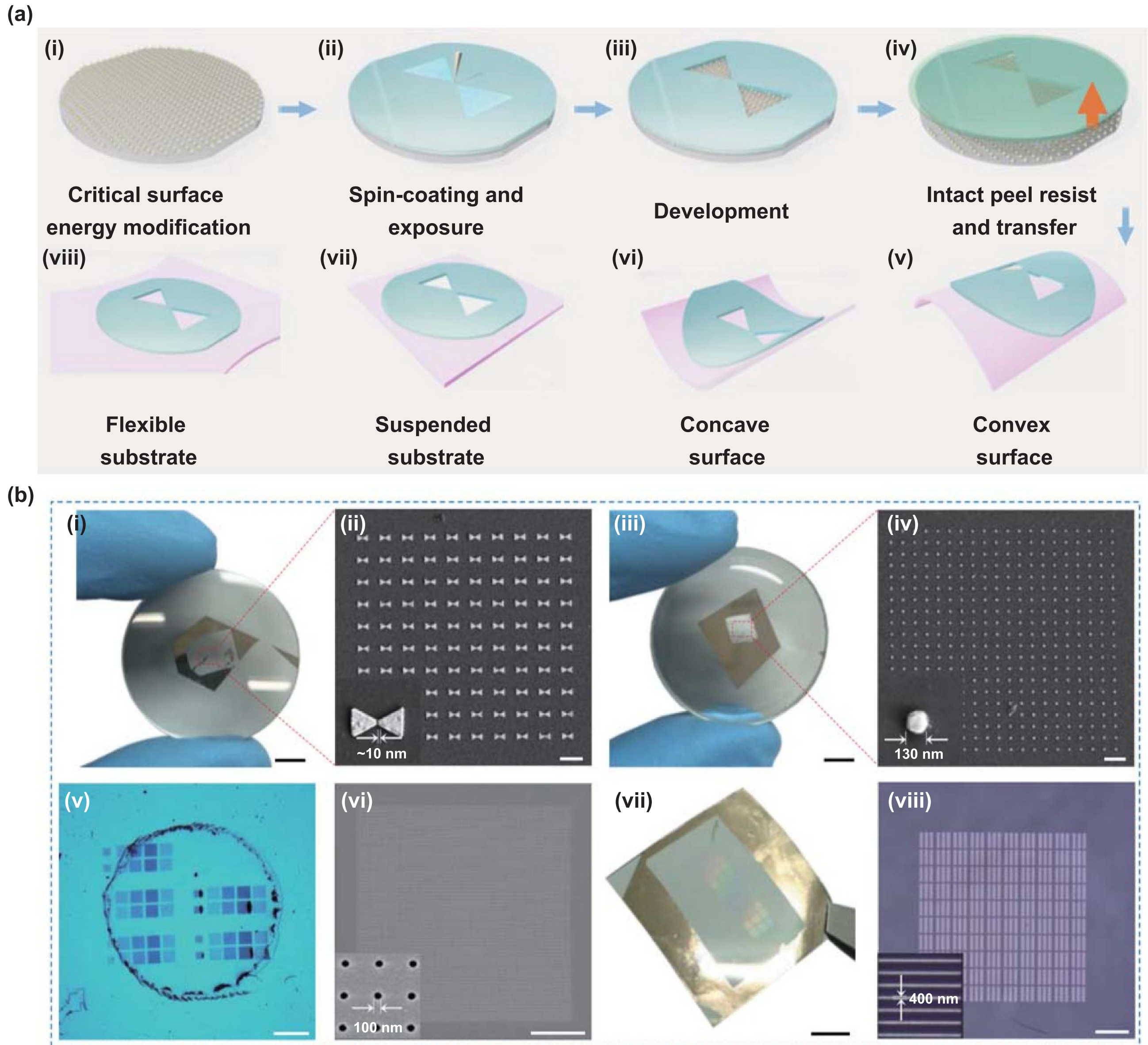

Figure 5. Demonstration of reliable *in situ* fabrication of multiscale gold structures onto an arbitrary receiver substrate. (a) Schematic illustration of the nanostencil mask: (i) surface modification to achieve critical surface energy interval; (ii) spin-coating of PMMA and exposure; (iii) development; (iv) intact peeling of the patterned PMMA resist for transfer; (v–viii) transfer of the patterned PMMA resist to difficult-to-process substrates, such as a convex surface, concave surface, suspended substrate, and flexible and stretchable substrates. (b) Optical and SEM micrographs of multiscale gold nanostructures after being transferred onto arbitrary surfaces: (i, ii) gold-bowtie array on a convex lens; (iii, iv) gold disk array on a concave lens; (v, vi) free-standing nanoholes on a suspended substrate; and (vii, viii) nanograting on flexible PDMS. Scale bars: 2 μm in (b-ii), (b-iv), 20 μm in (b-vi), 200 μm in (b-v), (b-viii), and 5 mm in (b-i), (b-iii), (b-vii).

no extra alignment marks or procedures are needed to ensure a highly accurate alignment between shapes of different sizes, making it simpler and lower cost than existing approaches.

Another advantage of this resist-based nTP technique is its unique capability to rapidly define wafer-scale metal-electrode arrays for use in high-performance devices, as shown in figure 6(c). Furthermore, this *ex situ* and all-dry lithography technique can avoid the introduction of defects in sensitive materials by high-energy beams during exposure, as well as residues and defects caused by solvents (organic or water) on the surface of materials during development, especially for functional 2D semiconductors (e.g. graphene [50], MoS_2 [51], $MoTe_2$ [52], and perovskites [53]). For example, we fabricated an array of chemical-vapor-deposited MoS_2 transistors with *in situ* nanogap electrodes (figures 6(d), S18, S19). The optical characterization is shown in figure S20. The *in situ* deposition method ensures high-quality metal–semiconductor contact and achieves ohmic contact (figures S21 and S22). Figures 6(e)–(i) shows a specific mechanically exfoliated MoS_2 transistor on a SiO_2/Si substrate with an *in situ* gold-nanogap electrode. The SEM micrograph inset shows a channel length of 380 nm. Our strategy is specifically

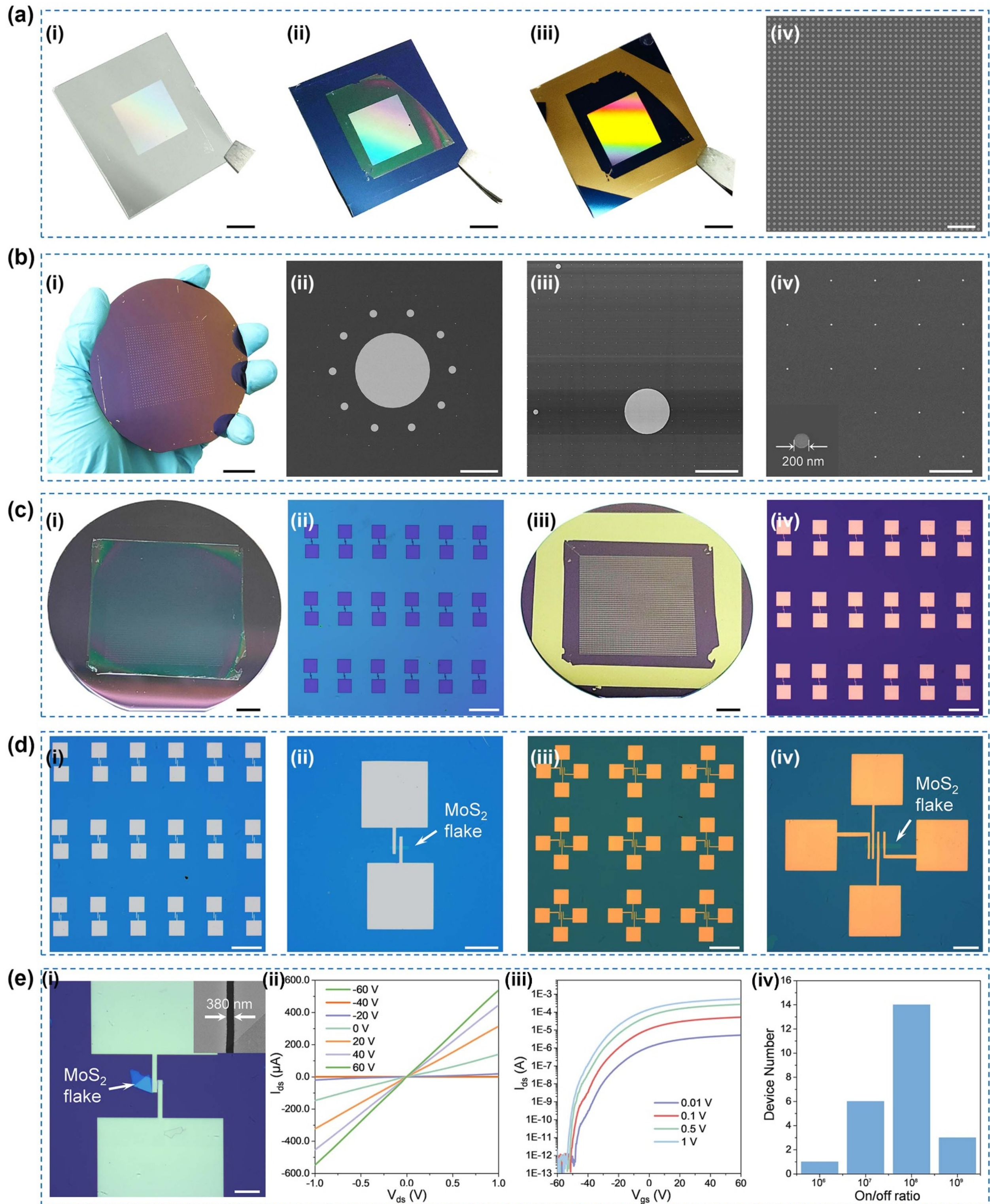

Figure 6. Massive, large-area, multiscale functional nanostructures fabricated using our resist-based nTP approach and contour exposure for optoelectronic device applications. (a) Demonstration of efficient preparation of massive structures: (i) PMMA pattern/PDMS laminate; (ii) the PMMA pattern on a SiO_2/Si substrate; (iii, iv) overview and details of the fabricated gold-disk array, for which the disk diameter was 2 μm and the period was 4 μm. (b) Overview and details of multiscale gold disks on a 4-inch SiO_2/Si wafer for disk diameters of 200 nm, 2 μm, 20 μm, and 100 μm. (c) Fabrication of a 2-inch wafer-scale metal-electrode array: (i, ii) electrode pattern in PMMA nanofilm; (iii, iv) details of the fabricated gold-electrode array after the peeling of PMMA. (d) Overview and details of chemical-vapor-deposited MoS_2 transistors with transferred two-terminal gold nanogap electrodes on a SiO_2/Si substrate. (e) Specific mechanically exfoliated MoS_2 transistor and its electrical properties: (i) morphological characterization of the transistor with a channel of 380 nm; (ii) the I_{ds}–V_{ds} output curves of the MoS_2 device under different gate voltages from −60 V to 60 V; (iii) the I_{ds}–V_{ds} curves with different source-drain bias voltages; (iv) statistic histogram of the ON/OFF ratio of 24 MoS_2 transistors with different channel lengths on a SiO_2/Si substrate. Scale bars: 5 μm in (b-iv), 20 μm in (b-iii) and (e-i), 20 μm in (a-iv) and (d-ii), (d-iv), 100 μm in (b-ii), 200 μm in (c-ii), (c-iv) and (d-i), (d-iii), 5 mm in (a-i)–(a-iii) and (c-i), (c-iii), and 2 cm in (b-i).

tailored to achieve near-zero adhesion, enabling intact stripping of the nanostencil electrode mask without breakage, even when the channel width is reduced below 500 nm, as shown in figure S23. The quality and thickness of the MoS_2 flakes were evaluated using Raman spectroscopy and AFM. The results in figure S24 indicate that the MoS_2 flakes comprised about seven layers.

In figure 6(e-ii), the linear I_{ds}–V_{ds} output curves indicate that the contact in the gold–MoS_2 junctions is an ohmic contact. Figure 6(e-iii) shows the I_{ds}–V_{ds} curves with different source–drain bias voltages. An ON-state gate voltage (V_{gs}) of less than 0 V indicates that the transistor in contact with the gold electrodes shows n-type behavior as a result of the defect states in the MoS_2/SiO_2 interface or because of intrinsic defects of sulfur atoms in the exfoliated MoS_2 [7]. The ON/OFF ratio of the fabricated MoS_2 transistor remained at a high level of 1.2×10^9 at a V_{ds} of 1 V (figure 6(e-iii)), demonstrating the high performance of the devices fabricated with our approach. Statistical analysis of the results from 24 MoS_2 transistors reveals that the ON/OFF ratio of most fabricated MoS_2 devices was maintained at $\sim 10^8$ (figure 6(e-iv)), which is sufficiently stable and reliable for use in electronic device applications. We note that the ON/OFF ratio of the devices can be tuned by various parameters, including the thickness of the exfoliated MoS_2 and the channel length, which are dominated by the transferred gold-nanogap electrodes (table S2).

3. Conclusions

We have demonstrated an innovative and effective approach to realizing a critical surface energy interval to achieve near-zero adhesion. This enabled the *in situ* fabrication of large-area, functional nanostructures and optoelectronic devices on difficult-to-process substrates, overcoming inherent shortcomings of existing direct-transfer processes. Through molecular modification, the donor substrate achieved a critical surface energy interval, which enabled spin-coating and intact peeling of wafer-scale resist nanofilms. We studied the mechanism of how the molecules create critical modification and control the interface adhesion to allow reliable transfer printing of resist films and nanostructures based on wettability measurements and mechanical analysis. We showed that this technique is effective and reliable for all-dry peeling-and-releasing processes for a wafer-scale resist nanofilm (i.e. a nanostencil mask with high yield, 10 nm resolution, high throughput, and high quality). We also demonstrated that this method is effective for transferring various functional nanostructures, 3D-stacked multilayer nanofilms, and MoS_2-based optoelectronic devices onto diverse receiver substrates, including rigid, flexible, curved surfaces, and even suspended substrates. Our method has the potential to facilitate monolithic integration of nanoscale functional materials with next-generation nanophotonic and electronic devices on arbitrary substrates on an even larger scale than that demonstrated in this work [54].

4. Experimental section

Implementation of the critical surface energy interval and near-zero adhesion on a donor wafer: The cleaned 4-inch silicon wafer and Petri dish containing 120 μl of OTS solution were placed in a vacuum vessel in which the vacuum value was set to 12 psi. By controlling the modification time at room temperature, the OTS layer with different surface-absorption statuses, such as insufficient absorption (4–6 min), critical absorption (8–10 min), and excessive absorption (>15 min), could be covered on the entire surface of the silicon wafer through Si–O–Si bonding. The OTS-rendered silicon wafer was then rinsed in ample isopropanol (IPA) for 1 min and dried with compressed N_2. Thereafter, several thicknesses of PMMA nanofilm were completely spin-coated onto the samples, which was aided by the minimal adhesion force. After treatment at 180 °C for 5 min on a hotplate, a reliable sandwich structure (i.e. PMMA nanofilm/critical OTS-modified layer/silicon) was obtained.

Intact peeling and transfer printing of nanofilms: A large-scale commercial PDMS stamp (thickness: 500 μm) was directly covered over the PMMA nanofilm to form a new laminate in which the adhesion of the interface depended only on the van der Waals forces. Subsequently, the PDMS/PMMA laminate was completely peeled from the donor substrate by applying an external mechanical force at an angle of 45° at room temperature. Thereafter, the laminate (i.e. PDMS-supported PMMA nanofilms) was printed directly on the arbitrary receiver substrates. After 5 min of heating (100 °C) on a hotplate, the modification-free PDMS stamp was automatically released owing to the differences in the thermal expansion coefficient and elastic moduli of the materials (i.e. PDMS and the receiver substrate). Finally, the large-scale PMMA films without cracks, wrinkles, or deletions were transferred onto arbitrary surfaces. The following parameters were used for the mechanical force test: tape width of 15 mm, peeling displacement of 10 mm, and peeling speed of 10 mm·s^{-1}.

EBL: A PMMA (950 kDa, A3, Allresist GmbH) resist was spin-coated on an OTS-modified substrate. To better perform the subsequent stripping process, a double layer of PMMA (950 kDa (top)/495 kDa (bottom)) resist was selectively spin-coated on the modified substrate. Then, the sample was prebaked on a hotplate at 180 °C for 5 min. The exposure was performed using an EBL system (Raith-150Two) with an accelerating voltage of 30 kV and a beam current of 1260 pA. The area dose ranged from 200 to 300 μC·cm^{-2}, and the line dose ranged from 800 to 3000 pC·cm^{-1}. After the e-beam exposure, the resist was developed for 60 s, finished by a thorough rinse in IPA solution for 60 s.

Metal deposition: Samples containing the PMMA pattern were transferred into a thermal evaporator (JSD300, Anhui Jiashuo Vacuum Technology Co. Ltd) for Cr, Au, and Ag deposition. 2 nm thick Cr was used to adhere the Au antennas to the substrate and determine the contact with MoS_2.

Characterization: Morphology characterization was conducted using field-emission SEM (SIGMA-HD, Carl-ZEISS) and AFM (Bruker, Dimension Icon). Raman and photoluminescence measurements were characterized using a confocal microscopic system (WITec alpha300 R), with excitation from a 532 nm laser with a power of 50 μW. The integration time was set as 4 s. The transmission spectra of the fabricated devices were measured using a home-built microarea transmission spectrometer. The electrical characteristics of the transistors were measured using a Lakeshore PS100 probe station and a Keysight B1500A semiconductor parameter analyzer.

Numerical simulations: Optical spectra were calculated using the Finite Difference Time Domain (FDTD) simulator supplied by the Lumerical software package (3D-FDTD). The refractive index or permittivity of the materials used in this work was taken from the material database in the FDTD solution supplied by Lumerical Ltd (the refractive index of the PMMA resist was set to 1.486). In all simulations, the periodic boundary condition was adopted along both the x- and y-axes, and perfectly matched layers were used along the propagation directions. A quasi-static model was built to simulate the peeling process by using commercial finite-element analysis software (ABAQUS 2019). The elastic modulus (E) and Poisson's ratio (v) of PDMS and PMMA were $E_{\text{PDMS}} = 800$ kPa and $v_{\text{PDMS}} = 0.48$ [55], $E_{\text{PMMA}} = 3$ GPa and $v_{\text{PMMA}} = 0.35$ [56], and $E_{\text{Substrate}} = 200$ GPa and $v_{\text{Substrate}} = 0.2$.

Acknowledgments

Z S and B F contributed equally to this work. This work was supported by the National Key Research and Development Program of China (No. 2022YFB4602600), the National Natural Science Foundation of China (No. 52221001), and Hunan Provincial Innovation Foundation for Postgraduate (No. CX20220406).

Conflict of interest

The authors declare no conflict of interest.

ORCID iD

Huigao Duan https://orcid.org/0000-0001-9144-2864

References

[1] Takei K, Takahashi T, Ho J C, Ko H, Gillies A G, Leu P W, Fearing R S and Javey A 2010 Nanowire active-matrix circuitry for low-voltage macroscale artificial skin *Nat. Mater.* **9** 821–6
[2] Kim D H *et al* 2010 Dissolvable films of silk fibroin for ultrathin conformal bio-integrated electronics *Nat. Mater.* **9** 511–7
[3] Aksu S, Huang M, Artar A, Yanik A A, Selvarasah S, Dokmeci M R and Altug H 2011 Flexible plasmonics on unconventional and nonplanar substrates *Adv. Mater.* **23** 4422–30
[4] Meitl M A, Zhu Z T, Kumar V, Lee K J, Feng X, Huang Y Y, Adesida I, Nuzzo R G and Rogers J A 2006 Transfer printing by kinetic control of adhesion to an elastomeric stamp *Nat. Mater.* **5** 33–38
[5] Sekitani T, Zschieschang U, Klauk H and Someya T 2010 Flexible organic transistors and circuits with extreme bending stability *Nat. Mater.* **9** 1015–22
[6] Rogers J A, Someya T and Huang Y G 2010 Materials and mechanics for stretchable electronics *Science* **327** 1603–7
[7] Chen Y Q, Shu Z W, Feng Z Y, Kong L A, Liu Y and Duan H G 2020 Reliable patterning, transfer printing and post-assembly of multiscale adhesion-free metallic structures for nanogap device applications *Adv. Funct. Mater.* **30** 2002549
[8] Xue Z G *et al* 2022 Assembly of complex 3D structures and electronics on curved surfaces *Sci. Adv.* **8** eabm6922
[9] Zhao H B *et al* 2022 Mechanically guided hierarchical assembly of 3D mesostructures *Adv. Mater.* **34** 2109416
[10] Kim T H *et al* 2011 Full-colour quantum dot displays fabricated by transfer printing *Nat. Photon.* **5** 176–82
[11] Loh G H 2008 3D-stacked memory architectures for multi-core processors *ACM SIGARCH Comput. Archit. News* **36** 453–64
[12] Kum H S *et al* 2020 Heterogeneous integration of single-crystalline complex-oxide membranes *Nature* **578** 75–81
[13] Fan Z Y, Ho J C, Jacobson Z A, Razavi H and Javey A 2008 Large-scale, heterogeneous integration of nanowire arrays for image sensor circuitry *Proc. Natl Acad. Sci. USA* **105** 11066–70
[14] Davanco M, Liu J, Sapienza L, Zhang C Z, De Miranda Cardoso J V, Verma V, Mirin R, Nam S W, Liu L and Srinivasan K 2017 Heterogeneous integration for on-chip quantum photonic circuits with single quantum dot devices *Nat. Commun.* **8** 889
[15] Zheng C Q, Shen Y, Liu M K, Liu W J, Wu S Y and Jin C J 2019 Layer-by-layer assembly of three-dimensional optical functional nanostructures *ACS Nano* **13** 5583–90
[16] Zhu Z J, Guo S Z, Hirdler T, Eide C, Fan X X, Tolar J and McAlpine M C 2018 3D printed functional and biological materials on moving freeform surfaces *Adv. Mater.* **30** 1707495
[17] Wu L X, Meng L, Wang Y Y, Lv M, Ouyang T Y, Wang Y L and Zeng X Y 2023 Fabrication of polyetheretherketone (PEEK)-based 3D electronics with fine resolution by a hydrophobic treatment assisted hybrid additive manufacturing method *Int. J. Extrem. Manuf.* **5** 035003
[18] Yi N, Gao Y Y, Verso A L Jr, Zhu J, Erdely D, Xue C L, Lavelle R and Cheng H Y 2021 Fabricating functional circuits on 3D freeform surfaces via intense pulsed light-induced zinc mass transfer *Mater. Today* **50** 24–34
[19] Luo H, Zhang Y Y, Yu J W, Dong X R and Zhou T F 2023 Additive, subtractive and formative manufacturing of glass-based functional micro/nanostructures: a comprehensive review *Mater. Des.* **233** 112285
[20] Nagel R D, Haeberle T, Schmidt M, Lugli P and Scarpa G 2016 Large area nano-transfer printing of sub-50-nm metal nanostructures using low-cost semi-flexible hybrid templates *Nanoscale Res. Lett.* **11** 143
[21] Zhao Z J, Shin S H, Lee S Y, Son B, Liao Y K, Hwang S, Jeon S, Kang H, Kim M and Jeong J H 2022 Direct chemisorption-assisted nanotransfer printing with wafer-scale uniformity and controllability *ACS Nano* **16** 378–85
[22] Jeong J W *et al* 2014 High-resolution nanotransfer printing applicable to diverse surfaces via interface-targeted adhesion switching *Nat. Commun.* **5** 5387
[23] Yim S, Jeon S, Kim J M, Baek K M, Lee G H, Kim H, Shin J and Jung Y S 2018 Transferrable plasmonic Au thin film

containing sub-20 nm nanohole array constructed via high-resolution polymer self-assembly and nanotransfer printing *ACS Appl. Mater. Interfaces* **10** 2216–23
[24] Liu W J, Zou Q S, Zheng C Q and Jin C J 2019 Metal-assisted transfer strategy for construction of 2D and 3D nanostructures on an elastic substrate *ACS Nano* **13** 440–8
[25] Li H, Wu J, Huang X, Yin Z Y, Liu J Q and Zhang H 2014 A universal, rapid method for clean transfer of nanostructures onto various substrates *ACS Nano* **8** 6563–70
[26] Yan Z C *et al* 2017 Thermal release transfer printing for stretchable conformal bioelectronics *Adv. Sci.* **4** 1700251
[27] Carlson A, Bowen A M, Huang Y G, Nuzzo R G and Rogers J A 2012 Transfer printing techniques for materials assembly and micro/nanodevice fabrication *Adv. Mater.* **24** 5284–318
[28] Schneider G F, Calado V E, Zandbergen H, Vandersypen L M K and Dekker C 2010 Wedging transfer of nanostructures *Nano Lett.* **10** 1912–6
[29] Bian J, Zhou L B Y, Wan X D, Zhu C, Yang B and Huang Y A 2019 Laser transfer, printing, and assembly techniques for flexible electronics *Adv. Electron. Mater.* **5** 1800900
[30] Luo H Y, Wang C J, Linghu C H, Yu K X, Wang C and Song J Z 2020 Laser-driven programmable non-contact transfer printing of objects onto arbitrary receivers via an active elastomeric microstructured stamp *Natl Sci. Rev.* **7** 296–304
[31] Haisma J and Spierings G A C M 2002 Contact bonding, including direct-bonding in a historical and recent context of materials science and technology, physics and chemistry: historical review in a broader scope and comparative outlook *Mater. Sci. Eng.* R **37** 1–60
[32] Schmidt M A 1998 Wafer-to-wafer bonding for microstructure formation *Proc. IEEE* **86** 1575–85
[33] Liu G Y *et al* 2022 Graphene-assisted metal transfer printing for wafer-scale integration of metal electrodes and two-dimensional materials *Nat. Electron.* **5** 275–80
[34] Chen F R *et al* 2022 Mass transfer techniques for large-scale and high-density microLED arrays *Int. J. Extrem. Manuf.* **4** 042005
[35] Liao W S, Cheunkar S, Cao H H, Bednar H R, Weiss P S and Andrews A M 2012 Subtractive patterning via chemical lift-off lithography *Science* **337** 1517–21
[36] Jeong S H, Zhang S, Hjort K, Hilborn J and Wu Z G 2016 PDMS-based elastomer tuned soft, stretchable, and sticky for epidermal electronics *Adv. Mater.* **28** 5830–6
[37] Song W J, Kong L G, Tao Q Y, Liu Q, Yang X D, Li J, Duan H G, Duan X D, Liao L and Liu Y 2021 High-resolution van der Waals stencil lithography for 2D transistors *Small* **17** 2101209
[38] Liu Y, Guo J, Zhu E B, Liao L, Lee S J, Ding M N, Shakir I, Gambin V, Huang Y and Duan X F 2018 Approaching the Schottky–Mott limit in van der Waals metal–semiconductor junctions *Nature* **557** 696–700
[39] Feng X, Meitl M A, Bowen A M, Huang Y G, Nuzzo R G and Rogers J A 2007 Competing fracture in kinetically controlled transfer printing *Langmuir* **23** 12555–60
[40] Chen X S, Xu Z Y, Wu K J, Zhang S N, Li H W, Meng Y C, Wang Z W, Li L Q and Ma X M 2016 Facile peeling method as a post-remedy strategy for producing an ultrasmooth self-assembled monolayer for high-performance organic transistors *Langmuir* **32** 9492–500
[41] Cheng C Y, Hong F C N and Huang C Y 2010 Micro-and nanopatterned polymethylmethacrylate layers on plastic poly (ethylene terephthalate) substrates by modified roller-reversal imprint process *J. Vac. Sci. Technol.* B **28** 921–5
[42] Hong F C N and Kao Y C 2011 Residual-layer-free printing by selective filling of self-assembled monolayer-treated mold *J. Vac. Sci. Technol.* B **29** 041601
[43] Zhang X, Shi F, Niu J, Jiang Y G and Wang Z Q 2008 Superhydrophobic surfaces: from structural control to functional application *J. Mater. Chem.* **18** 621–33
[44] Wang M J, Liechti K M, Wang Q and White J M 2005 Self-assembled silane monolayers: fabrication with nanoscale uniformity *Langmuir* **21** 1848–57
[45] Tang L Z and Lee N Y 2010 A facile route for irreversible bonding of plastic-PDMS hybrid microdevices at room temperature *Lab Chip* **10** 1274–80
[46] Yang Z M, Chen Y Q, Zhou Y M, Wang Y S, Dai P, Zhu X P and Duan H G 2017 Microscopic interference full-color printing using grayscale-patterned Fabry–Perot resonance cavities *Adv. Opt. Mater.* **5** 1700029
[47] Liu Q, Chen Y Q, Feng Z Y, Shu Z W and Duan H G 2022 Resist nanokirigami for multipurpose patterning *Natl Sci. Rev.* **9** nwab231
[48] Chen Y Q, Shu Z W, Zhang S, Zeng P, Liang H K, Zheng M J and Duan H G 2021 Sub-10 nm fabrication: methods and applications *Int. J. Extrem. Manuf.* **3** 032002
[49] Chen Y Q, Xiang Q, Li Z Q, Wang Y S, Meng Y H and Duan H G 2016 “Sketch and peel” lithography for high-resolution multiscale patterning *Nano Lett.* **16** 3253–9
[50] Chen F, Xia J L, Ferry D K and Tao N J 2009 Dielectric screening enhanced performance in graphene FET *Nano Lett.* **9** 2571–4
[51] Late D J, Liu B, Matte H S S R, Dravid V P and Rao C N R 2012 Hysteresis in single-layer MoS_2 field effect transistors *ACS Nano* **6** 5635–41
[52] Qu D S, Liu X C, Huang M, Lee C, Ahmed F, Kim H, Ruoff R S, Hone J and Yoo W J 2017 Carrier-type modulation and mobility improvement of thin $MoTe_2$ *Adv. Mater.* **29** 1606433
[53] Yu W L *et al* 2018 Single crystal hybrid perovskite field-effect transistors *Nat. Commun.* **9** 5354
[54] Feng B, Chen Y F, Sun D, Yang Z Y, Yang B, Li X and Li T 2021 Precision integration of grating-based polarizers onto focal plane arrays of near-infrared photovoltaic detectors for enhanced contrast polarimetric imaging *Int. J. Extrem. Manuf.* **3** 035201
[55] Seghir R and Arscott S 2015 Extended PDMS stiffness range for flexible systems *Sens. Actuators* A **230** 33–39
[56] Chang J, Toga K B, Paulsen J D, Menon N and Russell T P 2018 Thickness dependence of the Young’s modulus of polymer thin films *Macromolecules* **51** 6764–70